Spermine induced reversible collapse of deoxyribonucleic acid-bridged nanoparticle-based assemblies

Göeken, Kristian L.; Schasfoort, Richard B.M.; Subramaniam, Vinod; Gill, Ron

published in
Nano Research
2018

DOI (link to publisher)
10.1007/s12274-017-1641-0

document version
Publisher's PDF, also known as Version of record

Nano Research 2018, 11(1): 383–396
https://doi.org/10.1007/s12274-017-1641-0
Research Article
ISSN 1998-0124
CN 11-5974/O4

Spermine induced reversible collapse of deoxyribonucleic acid-bridged nanoparticle-based assemblies

Kristian L. Göeken[1], Richard B. M. Schasfoort[1], Vinod Subramaniam[1,2], and Ron Gill[1,3] (✉)

[1] *MIRA Institute for Biomedical Technology and Technical Medicine, University of Twente, Drienerlolaan 5, 7522 NB Enschede, the Netherlands*
[2] *Vrije Universiteit Amsterdam, De Boelelaan 1105, 1081 HV Amsterdam, the Netherlands*
[3] *Saxion University of Applied Sciences, M. H. Tromplaan 28, 7513 AB Enschede, the Netherlands*

Received: 21 November 2016
Revised: 21 April 2017
Accepted: 23 April 2017

KEYWORDS

nanoparticles,
spermine,
deoxyribonucleic acid,
localized surface plasmon resonance,
surface plasmon resonance imaging

ABSTRACT

DNA-linked 2D and 3D nano-assemblies find use in a diverse set of applications, ranging from DNA-origami in drug delivery and medical imaging, to DNA-linked nanoparticle structures for use in plasmonics and (bio)sensing. However, once these structures have been fully assembled, few options are available to modulate structure geometry. Here, we investigated the use of the polycation spermine to induce DNA collapse in small oligonucleotide-linked (54 bp) gold nanoparticle structures by monitoring shifts in the localized surface plasmon resonance (LSPR) peak and by comparing the data with finite-difference time-domain (FDTD) simulations. Our data shows that low concentrations of spermine can be applied to induce large changes in DNA conformation, leading to a significant reduction in interparticle distance (from ~ 25 to ~ 3 nm) and enhanced plasmonic coupling. The DNA collapse is near-instantaneous and reversible, and its application at low and high DNA densities is demonstrated with surface plasmon resonance imaging (SPRi), showing the potential of spermine to dynamically modulate distances and geometry in DNA-based nano-assemblies.

1 Introduction

Recent advances in the hybridization-based assembly of intricate 2D and 3D nanostructures have renewed the interest in the use of DNA as a linker or spacer molecule [1]. This is in part due to the versatility of DNA as a building block, and the large amount of control it offers over initial structure geometry. Additionally, ubiquitous commercial DNA synthesis services and software for designing complex structures have resulted in the application of DNA in a wide range of fields. Examples include DNA-origami structures for encapsulation of drugs [2, 3], imaging modalities [4], enzymes (i.e., nanoreactors) [5], and DNA-templated nanoparticle constructs of varying scale [6, 7].

Address correspondence to r.gill@utwente.nl

DNA offers a limited degree of plasticity, which allows partial reshaping of structures post assembly. Although this plasticity is advantageous for the aforementioned examples, it is particularly useful in fields in which the geometry of the DNA-based assemblies strongly influences any emergent physical properties. Such is the case for DNA-coated metal nanoparticle assemblies used in plasmonic biosensing [8], surface-enhanced Raman spectroscopy (SERS) [9], and metal-enhanced fluorescence [10]. These fields make use of the unique optical properties of metal nanoparticles, which originate from interactions between light and coherently oscillating electrons, known as localized surface plasmons (LSPs) [11]. At their resonance frequencies, these oscillations give rise to strong scattering and absorption peaks [12]. These peaks occur in the visible region of the optical spectrum for most of the commonly used noble metal nanoparticles. The exact position of the resonance peak is governed by parameters such as particle size, shape, material, dielectric environment, and plasmonic coupling between nanoparticles [13]. Additionally, the localized surface plasmon resonance (LSPR) effect generates very potent local electric fields [14], which can be used to strongly enhance the fluorescence or scattering of molecules. By inserting these molecules between two or more nanoparticles, advantage can be taken of even stronger field enhancements in the hotspot, induced by plasmonic coupling [15]. The dynamic control over the distances between the molecules of interest and the nanoparticle(s) would allow switching of the local electric field enhancement, since it is strongly dependent on the distance between the molecule and the nanoparticle(s) [16].

In this article, we investigated the use of the polyamine spermine to alter distances between DNA-coated nanoparticles as a first step in creating such a field-enhancement switch. Polyamines are found in eukaryotic cells where they strongly interact with DNA [17]. These highly charged molecules can bind to the minor and/or major groove of DNA, thereby neutralizing the charge of the phosphodiester backbone, allowing DNA to collapse by taking on a more compact conformation [18]. The collapse is believed to be an all-or-nothing process that takes place when 90% of the phosphate charges are neutralized [19], and is a function of polyamine type, charge and, concentration [20, 21]. Additionally, besides the intramolecular effects, free DNA in solution [22] and DNA tethered to surfaces [23] have been observed to form intermolecular complexes due to the strong attractive forces induced between the DNA molecules after addition of a polyamine.

The biophysics behind the polyamine-induced collapse of large DNA molecules from natural sources has been extensively investigated. Examples include the collapse of T7 bacteriophage DNA (linear duplex, 40 kb) in solution, forming a particle with a hydrodynamic radius of 50 nm [24], and the formation of similarly sized toroidal or rod-like structures on mica substrates using collapsed λ-DNA (linear duplex, 50 kb) [25]. More recently, the collapse of smaller single DNA molecules (3 kb) tethered on two ends was modeled, predicting similar structures [26], and quartz crystal microbalance with dissipation monitoring (QCM-D) was used to show that changes in hydration occur upon the collapse of a small single stranded DNA (ssDNA) layer (59–184 bp) [27]. However, to our knowledge, no investigations have been performed on utilizing the collapse of individual small (< 60 bp), tethered duplex DNA by spermine to modulate interparticle distances in DNA-based nanoparticle constructs. In this article, we show that this biomimetic method can be used without the need for complex DNA sequences or special buffers and that the method is reversible, reproducible, and simple to use. This is in contrast to previous methods published in literature, which require either a tailored sequence or a target-dependent trigger (strand displacement [28–31], aptamers [32], and DNA-specific binding proteins [33]), cannot be used in physiological conditions (modifying ion concentrations [34, 35]), or have not been shown to be reversible (polyamidoamine dendrimers [36]). Distance-dependent plasmon coupling has been successfully applied in the past to determine the distances between gold nanoparticles [37]. By analysing the position of the plasmon coupled peak, interparticle distances can be estimated within the nanometer regime for a large range of nanoparticles [38]. With this tool in hand, we investigated the spermine-induced modulation of interparticle distances in two systems, namely nanoparticle core-satellite structures

and nanoparticle dimers. The investigation is performed at the ensemble level using a color camera, and at the individual-particle level using spectroscopy. The experimental results are compared to finite-difference time-domain (FDTD) simulations of nanoparticle dimers to estimate the changes in interparticle distance. Moreover, using nanoparticle-amplified surface plasmon resonance imaging (SPRi), we provide insights into the kinetics behind DNA collapse, and investigate its application at different DNA/nanoparticle surface densities.

2 Results and discussion

For the formation of the plasmonic nanostructures, 80 nm spherical gold nanoparticles (AuNPs) were deposited on aminosilane-modified glass substrates and subsequently, functionalized with single-stranded DNA. These particles were chosen for their sufficiently large scattering cross section, enabling facile dark-field microscopy and spectroscopic measurements without suffering from the excessive peak broadening that occurs with the use of larger particles due to radiative damping. Following this, complementary target ssDNA was hybridized to the ssDNA on the 80 nm AuNPs (80 AuNPs). The ssDNA-functionalized 40 nm colloidal AuNPs (40 AuNPs) were then introduced and hybridized to the target ssDNA on the 80 AuNPs, forming core-satellite (80–40 AuNP) complexes. The 40 nm particles were chosen because of their adequately strong plasmonic coupling upon complex formation, and their high colloidal stability relative to larger nanoparticles, which enables aggregate-free ssDNA functionalization. The successful formation of these nanoparticle complexes can be followed by monitoring the wavelength shift of the plasmon peak associated with AuNP–AuNP plasmon coupling. Under static excitation conditions, the strength of this coupling is predominantly governed by the distances between the particles in each complex formed. These distances are determined by the persistence length of the DNA bridging the nanoparticles. After the addition of spermine, the double stranded DNA (dsDNA) is expected to compact, reducing the persistence length and thereby, the interparticle distance, as shown schematically in Fig. 1. The reduced distance will lead to stronger plasmonic coupling between the nanoparticles, and an additional red shift of the plasmon resonance should occur.

First, a color camera was used to confirm the spectral shifts associated with the initial formation of the nanocomplexes. A color image was generated in hybridization buffer before and after incubating the 40 AuNPs, followed by washing with the same buffer. The absolute change in red, green, and blue (RGB) color channels of more than a thousand 80 AuNPs was then analyzed using a custom Matlab script (Fig. 2, black bars). At high target DNA concentrations, the ratio of the number of 40 nm satellites to their 80 nm cores is >> 1, while at lower target DNA concentrations, the ratio is << 1. This leads to the formation of complexes containing up to ten 40-nm satellites at 0.1 nM target

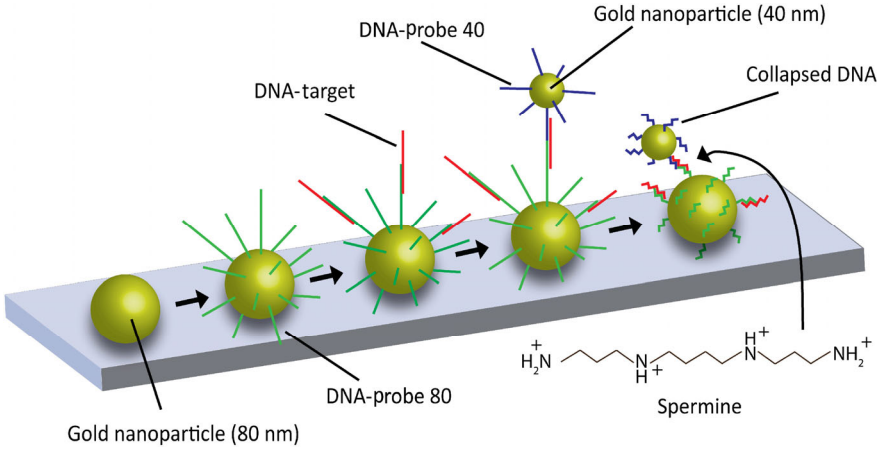

Figure 1 Schematic representation of the formation of a nanodimer. 80 nm spherical nanoparticles are deposited on glass, followed by ssDNA functionalization, target hybridization, complex formation, and spermine-induced DNA collapse.

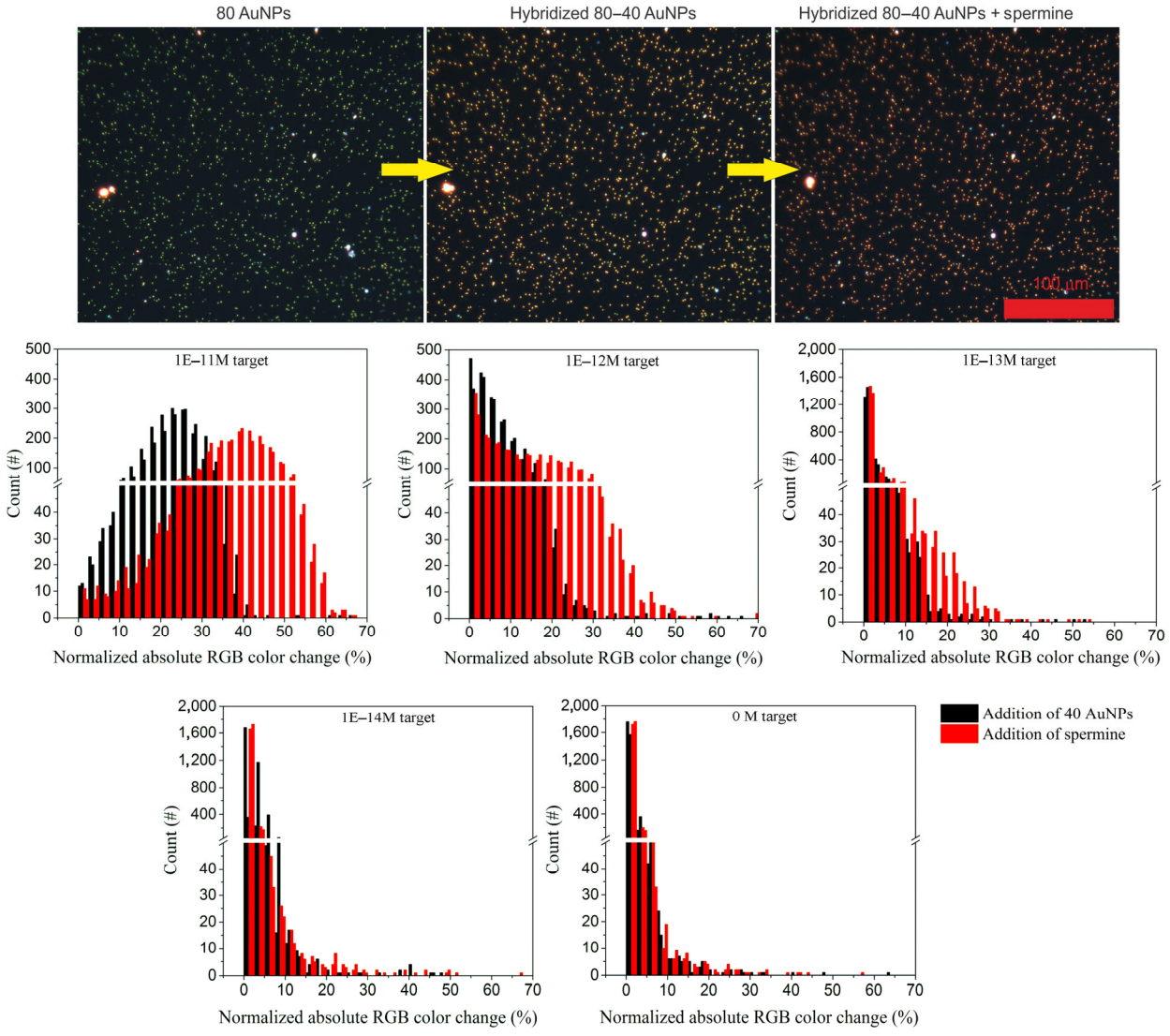

Figure 2 Top: Dark-field images showing single 80 AuNPs, hybridized 80–40 AuNPs at 0.1 nM target concentration, and the addition of 10 mM spermine to the hybridized 80–40 AuNP complexes. Bottom: Normalized absolute red, green, and blue color changes induced upon 40 AuNPs hybridization to 80 AuNPs (black bars), and upon incubation with 10 mM spermine (red bars). Each single bar represents one replicate (n = 2).

DNA and mostly unbound particles together with a few dimers at ≤0.1 pM target DNA. This was also previously confirmed in the Electronic Supplementary Material (ESM) of our previous paper on this nanoparticle satellite system [39]. In that article, scanning electron microscopy (SEM) was used to demonstrate that the average 80–40 AuNP complex formed at 0.1 nM target DNA has seven 40 nm satellites, whereas only dimers and single nanoparticles are found at 0.1 pM target DNA. The reduction in the number of 40 nm satellites per 80 nm core appears as diminishing changes in color, observed at successively lower target DNA concentrations. At 10 pM target DNA, over 98% of the 80 AuNPs show a > 5% shift in color, which is attributed to the specific hybridization between the 80 AuNPs and the 40 AuNPs. At 0 M target DNA, > 95% of all particles show a color shift less than 5%, which is attributed to camera noise and minor differences in focus which affect the measured RGB values. The values higher than 5% are likely caused by non-specific binding between the 40 and 80 nm AuNPs or incidental adsorption of strongly scattering dust particles. However, these events have a low occurrence rate and therefore do not pose a significant

problem for the analysis described in this paper. Next, hybridization buffer containing 10 mM spermine was added to the particles. Other researchers have shown that for the highly charged spermine molecule, collapse occurs at micromolar concentrations [22]. Consequently, this concentration of spermine should likely be more than sufficient to collapse all the DNA present in each nanocomplex. After incubation of the spermine, an additional shift in color compared to the original unbound image was observed (Fig. 2, red bars). This is consistent with a reduction in interparticle distance associated with spermine-induced DNA collapse. For the complexes formed at the highest concentration of target DNA (10 pM), the addition of spermine brought about a doubling in the average color shift. However, for the 80–40 AuNP complexes and dimers formed at lower target DNA concentration, the spermine-induced color shift was reduced. Intuitively, decreasing the distance between the core nanoparticle and several satellites should result in a stronger shift in color compared to merely a reduction in the distance between the two particles in each dimer. However, although the plasmonic coupling between multiple particles is much stronger at smaller distances, the effective size of the core-satellite structure also decreases.

Additionally, for the color of a symmetric structure, the red shift of one excitation axis can be opposed by the blue shift of the other excitation axis. Next, a spectrophotometer fiber-coupled to the dark-field microscope was used to investigate the change in resonance wavelength at the single-particle level. The effect of spermine was first studied in the high target DNA concentration regime (0.1 nM), which makes any reduction in interparticle distance by spermine-induced DNA collapse readily apparent, as shown by the color shift data. Figure 3 shows the effect of increasing concentrations of spermine in imaging buffer on five 80–40 AuNP complexes, and on a single uncoupled 80 AuNP. At low levels of spermine (10 μM) a small red shift is observed for the coupled particles, while no red shift is observed for uncoupled 80 AuNPs. The presence of bound target DNA without 40 AuNP satellites also showed no shift upon spermine addition (Fig. S1 in the ESM). Red shifts due to changes in the refractive index (RI) of the solution are expected to be minor, and only occur at very high concentrations of spermine since spherical particles exhibit low RI sensitivity [40]. The observed small red-shift at low spermine concentration can be explained by the decrease in the Debye length caused by the increase in charge screening due to the polyvalent spermine molecules in solution, and/or the induction of small

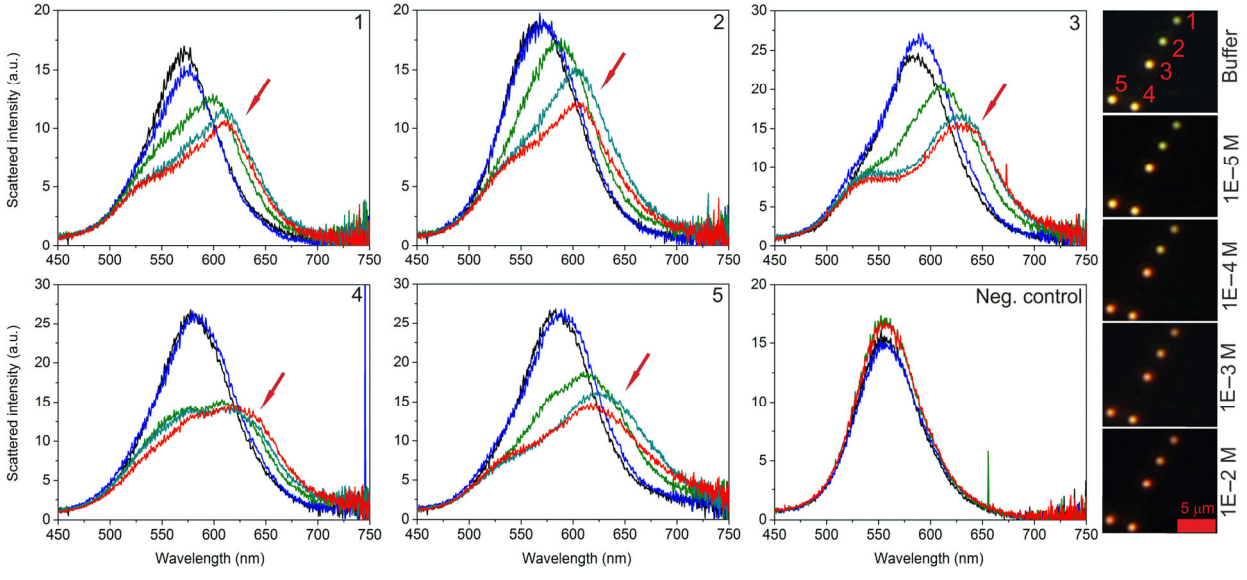

Figure 3 Measured scattering spectra and dark-field color images of 80–40 AuNP complexes (#1–5) formed at high target concentration (0.1 nM) in buffer containing increasing concentrations of spermine. Black line depicts buffer only. Blue, green, cyan, and red lines depict 10 μM, 100 μM, 1 mM, and 10 mM spermine in buffer, respectively. Negative control shows a single uncoupled 80 nm AuNP (not in the dark-field images). Red arrows denote state of full DNA collapse.

local bends in the DNA. This can lead to a limited decrease in interparticle distance, which is thought to occur at low concentrations of polycations [41]. Increasing the spermine concentration to 100 μM results in a strong decrease in scattering intensity, a large red shift of the main plasmon peak, as well as the appearance of an additional peak in the green region of the spectrum. This signifies a large decrease in interparticle distance, likely caused by the interaction of spermine with DNA causing (partial) collapse. The green peak is positioned around 550–560 nm, while the main peak is red-shifted from 570–580 nm to 610–640 nm. Increasing the spermine concentration to 1 mM brings about an additional red shift of the second peak by up to 10 nm, while the green peak remains at the same wavelength. Further increases in spermine concentration do not cause additional shifts, suggesting an end-state in the decrease in interparticle distance. The negative control is not affected by spermine concentrations as high as 10 mM, demonstrating that any collapse or change in conformation of the DNA attached to single 80 AuNPs does not contribute to the observed shifts in the plasmon peak. For the polyamine spermidine, counter-ions can compete for binding sites on the DNA [42], inhibiting DNA collapse. To investigate if a similar competition process occurs here, spermine was added to the buffer without sodium chloride. The low concentration of counter-ions resulted in the melting of a number of 80–40 AuNP complexes due to the decrease in electrostatic screening. However, for the remaining bound particles, the appearance of the two peaks was observed at a far lower spermine concentration (1 μM) (Fig. S2 in the ESM). This shows that the presence of sodium ions likely hinders the collapse of the hybridized DNA in a manner analogous to spermidine. Additionally, lowering the salt concentration in the presence of polyamines also increases the attractive potential between the ssDNA and/or dsDNA molecules [23] on the surface of the nanoparticle, which can also aid in the earlier onset of the collapse behavior as seen here.

To examine the reversibility of the collapsed state, the particles shown in Fig. 3 were washed several times in buffer without spermine. They were then measured directly after washing, and after incubation in the same buffer for 1 day. A blue shift upon washing the particles is observed, which corresponds to a reversion to larger interparticle distances (Fig. S3 in the ESM). However, the plasmon peaks were still slightly red-shifted compared to the original peak, indicating that either full extension did not immediately occur, or shifts in particle-particle orientation occurred upon collapse and extension. After prolonged incubation (up to 1 day) the plasmon peaks had returned to their approximate original positions, indicating near-reversibility, which is a known feature of multivalent cation-DNA interactions [43]. The slow decollapse rate observed in our measurements is most likely governed by the dissociation rate of spermine and not by the physical process of DNA unfolding itself [22].

As mentioned previously, the collapse or condensation of free DNA by spermine has been shown by other researchers to be an all-or-nothing effect at a threshold concentration of spermine [19] In contrast, our data shows a multiple-stage process causing intermediate red shifts between 0.01 and 1 mM spermine. This can be caused by full collapse of several hybridized strands in a stepwise manner due to a lack of sufficient spermine to neutralize enough of the phosphate backbone at lower concentrations of spermine. Alternatively, since the DNA in our system is tethered to a nanoparticle on both ends, only a limited degree of conformational freedom is available. This could result in a stepwise partial collapse of each individual strand over a wider concentration range of spermine since additional local energy minima are present, caused by a combination of factors such as the tension in the dsDNA strand, steric hindrance, and electrostatic repulsion between the nanoparticles themselves. To investigate both hypotheses, we performed a second set of experiments on a simplified system that contains only a few nanoparticle dimers and predominantly single nanoparticles. In this system, we can readily determine if stepwise collapse behavior still occurs for a single hybridized strand tethered between the nanoparticles of the dimer. Additionally, the variance in the position of the dimer relative to the 80 AuNP is much smaller than that of the 80–40 AuNp complexes, which can have plasmon-plasmon interactions that are difficult to interpret. Furthermore, the limited numerical aperture (NA) of our dark-field

objective is not able to pick up plasmonic modes that scatter preferentially away from the objective [44], which occur far less frequently for the dimers, since preferential attachment to the sides of the 80 AuNP has been observed previously [39].

This simpler nanoparticle (NP) system was prepared by lowering the target DNA concentration to 10 fM, which results in only < 5% bound particle dimers and > 95% single particles as seen previously in Fig. 2. These 80–40 AuNP dimers and single 80 AuNPs were then subjected to increasing concentrations of spermine as shown in Fig. 4. As with the larger complexes, a small red shift occurs in most cases at 10 μM spermine, which is not observed in the negative control. An increase in spermine concentration to 100 μM results in similar changes as observed previously with two peaks around 550–570 nm and 610–640 nm. However, at 1 mM spermine, shifts in the spectra still occur at varying degrees (such as particle #2 and #3). This demonstrates that conformational changes in a two-side tethered dsDNA occur over a much wider spermine concentration range than free DNA.

To evaluate the decrease in interparticle distance following DNA collapse, the well-known plasmon ruler technique [45] was applied. Although plasmon ruler equations are available in literature for a large range of NP shapes and sizes [38], it was necessary to model our specific setup as two heterogeneously sized gold spheres on a glass surface with a small surrounding shell of DNA for accurate results (Fig. S4 in the ESM).

We chose our modeled refractive index of 1.44 as a halfway point between water and a full monolayer of ssDNA [46], since the layer formed at 0.3 M NaCl is around 50% of the density of a full monolayer [47].

In the simulations, the interparticle distance d is varied, which determines the spectral position of the second peak. Additionally, we apply a weighting factor to the off- and on-axis excitations of the dimer (Fig. S5 in the ESM). The weighting factor originates from the differences in the binding position of the satellite in the 40–80 AuNP dimer relative to surface normal, since small differences in this position will strongly affect both the strength of the plasmon-plasmon coupled excitation mode as well as the intensity of the light scattered towards our objective lens. The spectra of the collapsed particles shown in Fig. 4 are plotted together with these simulated weighted averages at interparticle distances of 2 and 4 nm in Fig. 5.

It is apparent that the two peaks observed in the

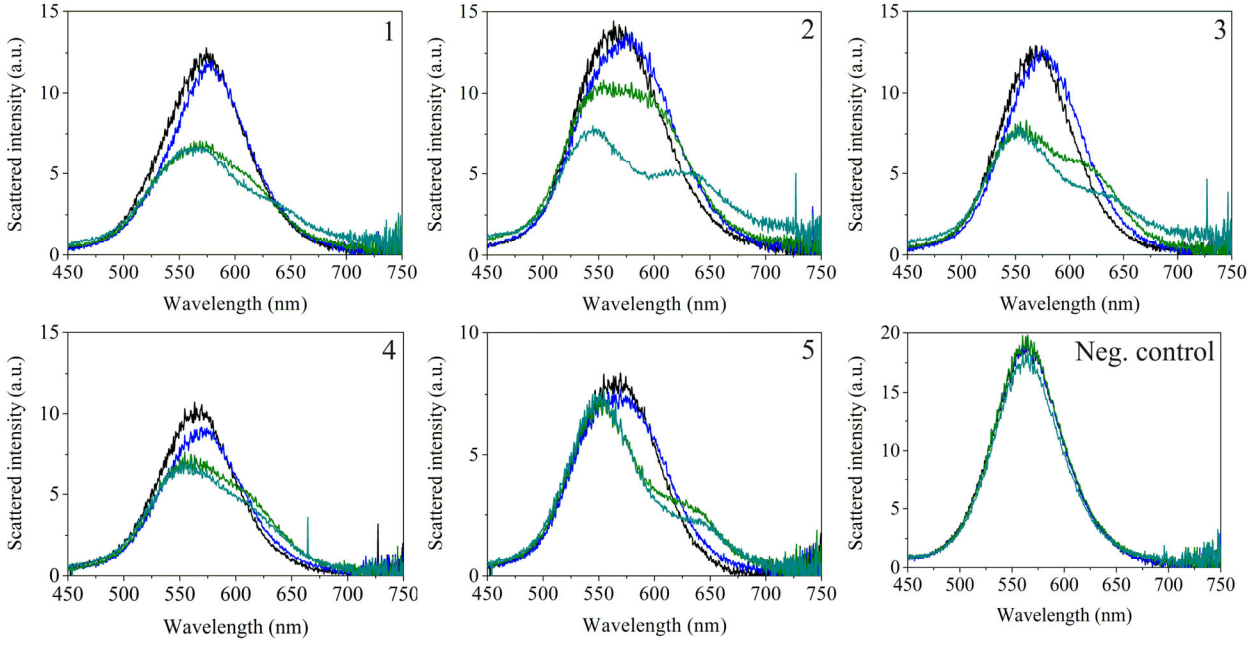

Figure 4 Measured scattering spectra of 80–40 AuNP dimers formed at low target concentration (10 fM) and a single uncoupled 80 AuNP (negative control). Particles were exposed to increasing concentrations of spermine in buffer. Black line depicts buffer only. Blue, green, and cyan lines depict 10 μM, 100 μM, and 1 mM spermine in buffer, respectively.

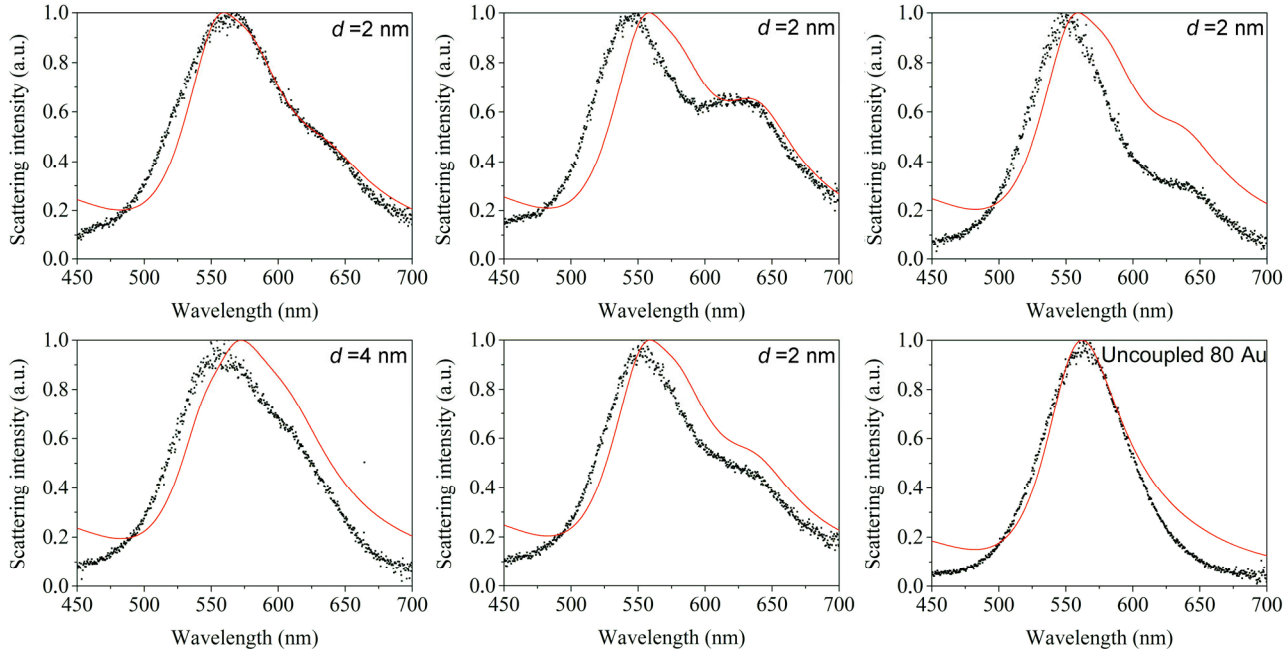

Figure 5 Normalized experimental spectra overlaid with simulated spectra for 80–40 AuNP dimers at interparticle distance d, and a single uncoupled 80 AuNP. Black points denote experimental data. Red line denotes corresponding simulated spectra.

experimental spectra are due to a combination of the red-shifted on-axis coupled dipole mode and the blue-shifted off-axis coupled mode as well as possible minor contributions from multipolar modes. Taken together, this only results in multiple discernible peaks at interparticle distances below ~ 5 nm. We observed that the peak around 550 nm (corresponding to the blue-shifted off-axis excitation mode) exhibits a stronger blue shift than that predicted by simulation for many of the nanoparticles. This might be due to dissimilarities in the actual size of the large particles used for these experiments, which have a coefficient of variation for their size distribution of 15%. Another possibility is that the blue shift is caused by the mismatch between the use of a fixed excitation angle in the simulations and the actual range of incidence angles of an annular light source [48]. This mismatch becomes increasingly relevant when dealing with structures larger than the quasi-static limit ($d > \lambda/10$) [49], which could also explain why the plasmon peak position of the single 80 AuNP is accurately predicted, while the ~ 550 nm peak position of most of the dimers shows divergence from the simulated data. However, it is clear that the main feature of the experimental spectra, which is the position of the red-shifted main peak, is predominantly caused by the interparticle distance d. This feature is accurately reproduced at interparticle distances between 2 and 4 nm, where the on-axis coupled resonance lies between 610 nm and 640 nm. This distance is comparable to that of two homogeneously sized 40 nm nanoparticles, where the ratio of the peak shift to the original single peak wavelength ($d\lambda/\lambda_0$) of 0.11–0.16 seen here, would match an interparticle distance of between 1 nm and 3 nm [38]. The total length of the DNA between particles is ~ 25 nm, however, only 19 nm is actually dsDNA, while the other 6 nm is a ssDNA adenine spacer. Adenine is well-known for having the highest binding affinity of all the bases to gold [50], making it likely that the adenine nucleotides are adsorbed on the gold, reducing the actual interparticle length to 19 nm, giving large compaction factors of 5× to 10×. A recent study determined the compaction percentage of a ssDNA layer deposited on a QCM-D quartz crystal to only be 1.3× [27]. However, in that specific study, the initial size of the DNA layer before the addition of spermine was already much smaller than the theoretical size (measured 12 nm in contrast to the expected 20 nm for 59 bp long DNA), reducing the compaction ratio from 2.3× to 1.3×. Furthermore, in that study, ssDNA

was tethered only on one side, while in our study, the ssDNA is tethered on two sides, inducing more tension in the strand. It has previously been proposed that the additional work that has to be performed against the tension forces opposing collapse induces a shorter, stepwise looping of the ssDNA strand, resulting in a much more compact collapsed DNA molecule [51]. Additionally, the collapse could also induce a hinge-like bending in the strand, bringing both particles closer together than would be possible with a strictly linear strand. It is also probable that DNA density plays a role in influencing the degree of compaction, since strong intermolecular forces between the ssDNA and/or the dsDNA are brought on by addition of spermine, which can induce additional axial or lateral forces.

To explore the collapse process further, surface plasmon resonance imaging was used to investigate the influence of dsDNA density on distance reduction and the associated spermine-induced collapse and extension kinetics. First, a layer of biotinylated ssDNA was deposited at successively lower surface densities on a streptavidin-coated planar gold surface. This layer was then hybridized to target DNA, followed by hybridization with 40 nm AuNP labels. Next, a buffer baseline was established, after which spermine was added. The sequential additions of target DNA, 40 nm AuNP labels and the addition and removal of spermine is shown in Fig. 6(a). The near-instantaneous amplification and the slower two-step attenuation of the SPRi response after washing can be unmistakably observed. The strong initial signal attenuation after washing indicates that most of the DNA extension occurs quickly, while the remaining part of the extension occurs over a much longer period of time. The SPRi response amplification of both the NP labeling and spermine follow a typical sigmoidal saturation-binding curve and can be fitted with the Hill equation [52] as shown in Figs. 6(b) and 6(c). However, the

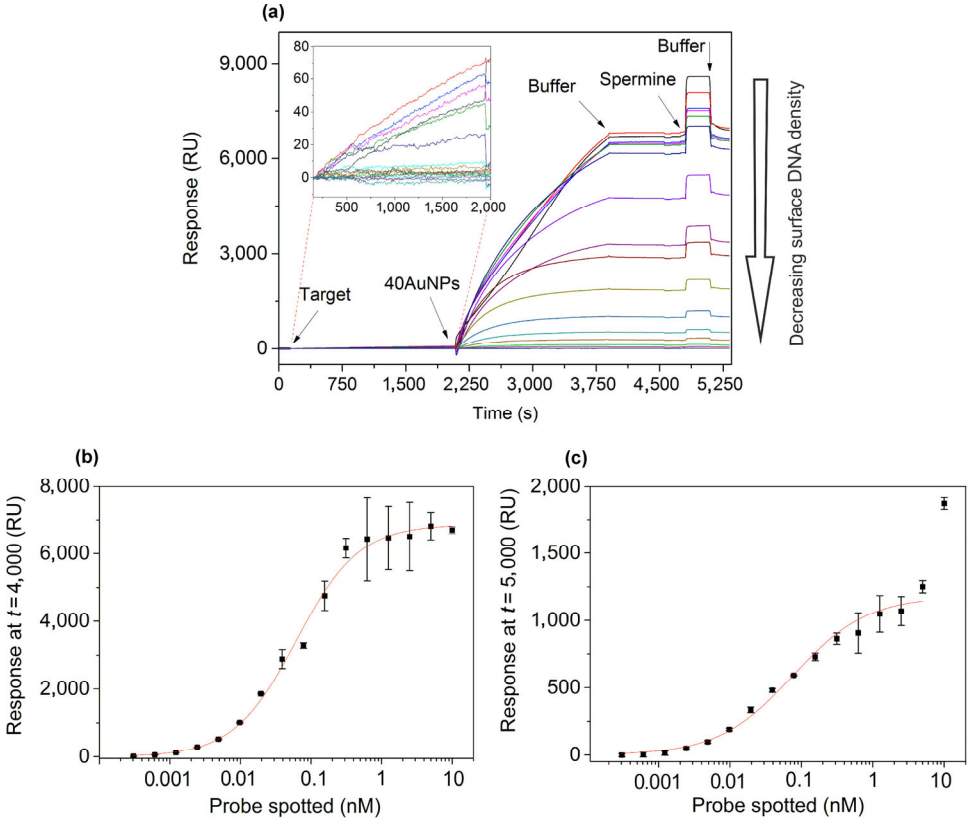

Figure 6 Average (n = 3) SPRi response of (a) target addition (inset shows magnification) ranging from 10 nM deposited biotin-DNA to 0.3 pM biotin-DNA, and subsequent nanoparticle amplification and spermine addition/removal (b) end-point after particle addition and washing and (c) response after spermine addition. Red curves are Hill equation fits (10 nM data point in (c) was omitted in the fit). Error bars in (b) and (c) are standard deviations (n = 3).

spermine-induced response at the highest two-surface densities is stronger than would be expected based on the previous data points, suggesting that at this density, possibly, other effects start to play a role, such as long range plasmonic coupling due to formation of larger structures (e.g. nanoparticle chains). Omitting these two data points, normalizing, and co-plotting the resulting Hill curves (Fig. S6, in the ESM) show that they are nearly identical, demonstrating that signal enhancement induced by the DNA collapse is directly related to the nanoparticle density on the surface. Additionally, the data indicates identical collapse and extension behavior of the aforementioned plasmonic nanoparticle core-satellite complexes, and no differences between the collapse mechanism at low and high DNA concentrations.

3 Conclusions

We report on a simple and fast method of strongly reducing the distances between DNA-hybridized nanoparticles by spermine-mediated DNA collapse. This method offers additional control over interparticle distances and the geometry of DNA-based nanostructures. DNA collapse occurs between 0.1 and 10 mM spermine at 50 mM NaCl, or at micromolar concentrations when no NaCl is present. The collapse results in strong plasmonic coupling between nanoparticles, and induces a red shift in plasmon peak wavelength. Estimations based on comparing the simulated data with the spectral data obtained by causing the collapse of single nanoparticle dimers, indicate a large reduction in the interparticle distance from ~ 19 nm to 2–4 nm, implying a potent decrease in DNA size. Using SPRi, we show that the effect of spermine is linear at both low and high DNA concentrations. Furthermore, we demonstrate that the collapse is near-instantaneous, and that the removal of spermine results in a two-phase extension process. The data presented here illustrates the application potential of spermine in modulating signals in DNA sensors based on plasmonic coupling, or in other areas such as plasmonic antennas or surface-enhanced fluorescence (SEF), where the "on-off" switching of interparticle distances by DNA collapse can be advantageous.

4 Methods

4.1 Reagents and instrumentation

Gold nanoparticles were purchased from nanoComposix (San Diego, USA). Sodium dodecyl sulfate (SDS), spermine, ethanol, hydrogen peroxide, tris(2-carboxyethyl)phosphine (TCEP), and sulfuric acid were purchased from Sigma-Aldrich (St. Louis, USA). (3-aminopropyl)triethoxysilane (APTES) was purchased from Fisher Scientific (Waltham, USA). Oligonucleotides were purchased from IBA GmbH (Göttingen, Germany) (for sequences see Table S1 in the ESM). Ultraviolet (UV)/ozone treatment was performed with a BioForce Nanosciences instrument. Spectroscopic measurements were taken with an Ocean Optics QE65000 spectrometer fiber-coupled to an inverted Olympus GX71 dark-field microscope. Color images were captured with a Zeiss Axiocam HRc color camera with a 20× NA 0.45 Olympus objective lens. spectral measurements were taken using a Tecan Infinite. SPRi was performed on an IBIS MX96 instrument (IBIS technologies, Enschede, The Netherlands). Spotting was done using a continuous flow microspotter (CFM) (Wasatch Microfluidics, Salt Lake City, USA) on a streptavidin-coated planar gold surface attached to a hemispherical prism (SensEye®, Ssens BV, Enschede, The Netherlands).

4.2 Coverslip preparation and nanoparticle deposition

Coverslips of thickness, 0.17 mm or 0.5 mm, were pre-cleaned with SDS (10% w/v), followed by copious washing with distilled water and cleaning in piranha solution (warning: extremely hazardous), and hydroxylation by UV/ozone treatment for 1 h. Slides were functionalized by immersion in ethanol containing APTES (1% v/v) for 30 min. Slides were rinsed with ethanol and double-distilled water (ddH_2O), followed by a curing step at 120 ℃ for minimally 15 h. 80 nm AuNPs were then deposited on the slides by immersion in 30× diluted stock 80 AuNP solution for 1 h. Afterwards, slides were cleaned with ddH_2O and UV/ozone to remove any residual APTES.

4.3 Nanoparticle DNA functionalization

40 AuNPs were functionalized as described elsewhere [39]. Briefly, thiolated oligonucleotides were reduced by TCEP and added to a concentrated solution of 40 nm gold nanoparticles. The solution was brought to pH 3 with trisodium citrate, after which, NaCl was added slowly over a period of 30 min. Particles were then washed five times (centrifugation for 12 min at 5,000 *g*, followed by removal of supernatant and resuspension in 10 mM 4-(2-hydroxyethyl)-1-piperazineethanesulfonic acid (HEPES) at pH 7.4). Successful functionalization without aggregation was confirmed by spectroscopy. 80 nm particles deposited on the APTES substrates were functionalized by the addition of reduced DNA (1 μM) in functionalization buffer (10 mM HEPES pH 7.4, 0.3 M NaCl and 0.1% SDS) for 90 min, followed by washing with the same buffer.

4.4 Nanoparticle complex formation

80–40 AuNP complexes and dimers were formed as follows: Target DNA was incubated with the 80 AuNPs at concentrations between 0.1 nM and 10 fM in hybridization buffer (10 mM HEPES pH 7.4, 1 M guanidinium thiocyanate, 70 mM NaCl and 0.1% Triton X-100) at 50 ˚C for 2 h. The wells were then washed 5× with washing buffer (10 mM HEPES pH 7.4, 0.3 M NaCl). Next, functionalized 40 AuNPs were added and allowed to hybridize to the 80 AuNPs. The wells were washed and re-imaged using the color camera to locate the particles that underwent a color shift, confirming the formation of bound complexes.

4.5 Spectroscopic measurements

Single 80 AuNPs, 80–40 AuNP dimers, and 80–40 AuNP complexes were monitored using both a spectroscope and the attached charge-coupled device (CCD) before and after washing the particles twice with imaging buffer (10 mM HEPES pH 7.4, 50 mM NaCl) containing spermine at different concentrations (10 mM to 0.1 μM). The camera integration time was set to 20 s. The spectrometer was background-corrected by the subtraction of a 20 second measurement with the microscope port closed. Lamp spectral correction was performed by imaging a white scattering surface (i.e., paper) and dividing the subsequent measurements by the correction spectrum.

4.6 SPRi measurements

For the SPRi measurements, biotinylated probe DNA was spotted at different concentrations (10 nM–0.3 pM) for 1 h in PBS (phosphate-buffered saline pH 7.4) containing Tween 20 (0.07%). Afterwards, the gold surface was washed with the same PBS solution and placed in the SPRi instrument. The following sequence was then followed: (1) washing with system buffer (10 mM HEPES pH 7.4, 0.3 M NaCl and 0.1% SDS), (2) 30 min incubation of target DNA (10 nM) in system buffer (120 μL), (3) 2 min washing with system buffer, (4) 30 min incubation of DNA-conjugated 40 AuNPs (1 OD) in system buffer, (5) 10 min washing with system buffer. The calibrated baseline response of each spot was set to zero before performing the subsequent steps. (6) 2 min incubation in low-salt system buffer (0.05 M NaCl instead of 0.3 M), (7) 1 min incubation in system buffer, (8) 5 min incubation with spermine (1 mM) in low-salt buffer, (9) 5 min washing with system buffer. Between each step, the system buffer was used to flush the remnants of the previous incubation step. The response of the DNA spots was adjusted by subtracting the calibrated signal of reference spots without DNA.

4.7 Finite-difference time-domain simulations

FDTD simulations were performed using a commercial software package (FDTD Solutions, Lumerical Solutions Inc.). Dielectric constants of gold were fitted to "Johnson and Christy" data points in the software. Mesh size was set to 1 nm. Boundaries were placed at a distance of at least a wavelength (1.5 μm) away from the particles to avoid spurious reflections. The angle of incidence was set obliquely (16°) to mimic the low contribution of the vertical component of the P-polarization in the signal captured by the dark-field objective lens. The glass surface was modeled as an infinite surface with the real part of the refractive index defined as RI = 1.47, independent of wavelength. The DNA was modeled as a 6 nm layer (RI = 1.44) on both the 80 nm as well as the

40 nm particles, because ssDNA is known to take on a brush-like conformation, which is smaller than its contour length. Coupled NPs were placed next to each other, parallel to the surface, and spacing was varied from 1–25 nm. Simulations were performed at both 0° (on the dimer axis) and 90° (perpendicular to the dimer axis) polarization, and the resulting spectra were given different weights (ranging from 4×–15× off-axis polarization). These spectra were then compared to experimentally acquired spectra of (collapsed) single 80–40 nm dimers.

Acknowledgements

This work was funded by the Dutch Technology Foundation STW (No. 11818). We would like to thank N. van der Velde for his assistance with the SPRi experiments.

Electronic Supplementary Material: Supplementary material (additional nanoparticle spectra, dark-field images, simulation data and DNA sequences) is available in the online version of this article at https://doi.org/10.1007/s12274-017-1641-0.

References

[1] Jones, M. R.; Seeman, N. C.; Mirkin, C. A. Programmable materials and the nature of the DNA bond. *Science* **2015**, *347*, 1260901.

[2] Zhan, P. F.; Jiang, Q.; Wang, Z. G.; Li, N.; Yu, H. Y.; Ding, B. Q. DNA nanostructure-based imaging probes and drug carriers. *ChemMedChem* **2014**, *9*, 2013–2020.

[3] Tintoré, M.; Eritja, R.; Fábrega, C. DNA nanoarchitectures: Steps towards biological applications. *ChemBioChem* **2014**, *15*, 1374–1390.

[4] Jungmann, R.; Avendaño, M. S.; Woehrstein, J. B.; Dai, M. J.; Shih, W. M.; Yin, P. Multiplexed 3D cellular super-resolution imaging with DNA-PAINT and exchange-PAINT. *Nat. Methods* **2014**, *11*, 313–318.

[5] Fu, Y. M.; Zeng, D. D.; Chao, J.; Jin, Y. Q.; Zhang, Z.; Liu, H. J.; Li, D.; Ma, H. W.; Huang, Q.; Gothelf, K. V. et al. Single-step rapid assembly of DNA origami nanostructures for addressable nanoscale bioreactors. *J. Am. Chem. Soc.* **2013**, *135*, 696–702.

[6] Samanta, A.; Banerjee, S.; Liu, Y. DNA nanotechnology for nanophotonic applications. *Nanoscale* **2015**, *7*, 2210–2220.

[7] Tan, S. J.; Campolongo, M. J.; Luo, D.; Cheng, W. L. Building plasmonic nanostructures with DNA. *Nat. Nanotechnol.* **2011**, *6*, 268–276.

[8] Petryayeva, E.; Krull, U. J. Localized surface plasmon resonance: Nanostructures, bioassays and biosensing—A review. *Anal. Chim. Acta* **2011**, *706*, 8–24.

[9] Thacker, V. V.; Herrmann, L. O.; Sigle, D. O.; Zhang, T.; Liedl, T.; Baumberg, J. J.; Keyser, U. F. DNA origami based assembly of gold nanoparticle dimers for surface-enhanced Raman scattering. *Nat. Commun.* **2014**, *5*, 3448.

[10] Chen, Y.; Munechika, K.; Ginger, D. S. Dependence of fluorescence intensity on the spectral overlap between fluorophores and plasmon resonant single silver nanoparticles. *Nano Lett.* **2007**, *7*, 690–696.

[11] Hutter, E.; Fendler, J. H. Exploitation of localized surface plasmon resonance. *Adv. Mater.* **2004**, *16*, 1685–1706.

[12] Willets, K. A.; Van Duyne, R. P. Localized surface plasmon resonance spectroscopy and sensing. *Annu. Rev. Phys. Chem.* **2007**, *58*, 267–297.

[13] Fong, K. E.; Yung, L. Y. L. Localized surface plasmon resonance: Aunique property of plasmonic nanoparticles for nucleic acid detection. *Nanoscale* **2013**, *5*, 12043–12071.

[14] Nien, L. W.; Lin, S. C.; Chao, B. K.; Chen, M. J.; Li, J. H.; Hsueh, C. H. Giant electric field enhancement and localized surface plasmon resonance by optimizing contour bowtie nanoantennas. *J. Phys. Chem. C* **2013**, *117*, 25004–25011.

[15] Woo, K. C.; Shao, L.; Chen, H. J.; Liang, Y.; Wang, J. F.; Lin, H. Q. Universal scaling and Fano resonance in the plasmon coupling between gold nanorods. *ACS Nano* **2011**, *5*, 5976–5986.

[16] Kang, K. A.; Wang, J. T.; Jasinski, J. B.; Achilefu, S. Fluorescence manipulation by gold nanoparticles: From complete quenching to extensive enhancement. *J. Nanobiotechnology* **2011**, *9*, 16.

[17] Mandal, S.; Mandal, A.; Johansson, H. E.; Orjalo, A. V; Park, M. H. Depletion of cellular polyamines, spermidine and spermine, causes a total arrest in translation and growth in mammalian cells. *Proc. Natl. Acad. Sci. U. S. A.* **2013**, *110*, 2169–2174.

[18] Feuerstein, B. G.; Pattabiraman, N.; Marton, L. J. Spermine-DNA interactions: Atheoretical study. *Proc. Natl. Acad. Sci. U. S. A.* **1986**, *83*, 5948–5952.

[19] Marquet, R.; Houssier, C.; Fredericq, E. An electro-optical study of the mechanisms of DNA condensation induced by spermine. *Biochim. Biophys. Acta* **1985**, *825*, 365–374.

[20] Pelta, J.; Livolant, F.; Sikorav, J. L. DNA aggregation induced by polyamines and cobalthexamine. *J. Biol. Chem.* **1996**, *271*, 5656–5662.

[21] Burak, Y.; Ariel, G.; Andelman, D. Competition between condensation of monovalent and multivalent ions in DNA aggregation. *Curr. Opin. Colloid Interface Sci.* **2004**, *9*, 53–58.

[22] Porschke, D. Dynamics of DNA condensation. *Biochemistry* **1984**, *23*, 4821–4828.

[23] Mertens, J.; Tamayo, J.; Kosaka, P.; Calleja, M. Observation of spermidine-induced attractive forces in self-assembled monolayers of single stranded DNA using a microcantilever sensor. *Appl. Phys. Lett.* **2011**, *98*, 153704.

[24] Wilson, R. W.; Bloomfield, V. A. Counterion-induced condensation of deoxyribonucleic acid. A light-scattering study. *Biochemistry* **1979**, *18*, 2192–2196.

[25] Lin, Z.; Wang, C.; Feng, X. Z.; Liu, M. Z.; Li, J. W.; Bai, C. L.The observation of the local ordering characteristics of spermidine-condensed DNA: Atomic force microscopy and polarizing microscopy studies. *Nucleic Acids Res.* **1998**, *26*, 3228–3234.

[26] Cortini, R.; Caré, B. R.; Victor, J. M.; Barbi, M. Theory and simulations of toroidal and rod-like structures in single-molecule DNA condensation. *J. Chem. Phys.* **2015**, *142*, 105102.

[27] Sun, L.; Frykholm, K.; Fornander, L. H.; Svedhem, S.; Westerlund, F.; Åkerman, B. Sensing conformational changes in DNA upon ligand binding using QCM-D. Polyamine condensation and rad51 extension of DNA layers. *J. Phys. Chem. B***2014**, *118*, 11895–11904.

[28] Zhang, D. Y.; Seelig, G. Dynamic DNA nanotechnology using strand-displacement reactions. *Nat. Chem.* **2011**, *3*, 103–113.

[29] Maye, M. M.; Kumara, M. T.; Nykypanchuk, D.; Sherman, W. B.; Gang, O. Switching binary states of nanoparticle superlattices and dimer clusters by DNA strands. *Nat. Nanotechnol.* **2010**, *5*, 116–120.

[30] Chen, J. I. L.; Chen, Y.; Ginger, D. S. Plasmonic nanoparticle dimers for optical sensing of DNA in complex media. *J. Am. Chem. Soc.* **2010**, *132*, 9600–9601.

[31] Lermusiaux, L.; Sereda, A.; Portier, B.; Larquet, E.; Bidault, S. Reversible switching of the interparticle distance in DNA-templated gold nanoparticle dimers. *ACS Nano* **2012**, *6*, 10992–10998.

[32] Lee, S. E.; Chen, Q.; Bhat, R.; Petkiewicz, S.; Smith, J. M.; Ferry, V. E.; Correia, A. L.; Alivisatos, A. P.; Bissell, M. J. Reversible aptamer-Au plasmon rulers for secreted single molecules. *Nano Lett.* **2015**, *15*, 4564–4570.

[33] Chen, J. I. L.; Durkee, H.; Traxler, B.; Ginger, D. S. Optical detection of protein in complex media with plasmonic nanoparticle dimers. *Small* **2011**, *7*, 1993–1997.

[34] Akiyama, Y.; Shikagawa, H.; Kanayama, N.; Takarada, T.; Maeda, M. Modulation of interparticle distance in discrete gold nanoparticle dimers and trimers by DNA single-base pairing. *Small* **2015**, *11*, 3153–3161.

[35] Lermusiaux, L.; Maillard, V.; Bidault, S. Widefield spectral monitoring of nanometer distance changes in DNA-templated plasmon rulers. *ACS Nano* **2015**, *9*, 978–990.

[36] Wang, H. Y.; Reinhard, B.M. Monitoring simultaneous distance and orientation changes in discrete dimers of DNA linked gold nanoparticles. *J. Phys. Chem. C* **2009**, *113*, 11215–11222.

[37] Sönnichsen, C.; Reinhard, B. M.; Liphardt, J.; Alivisatos, A. P. A molecular ruler based on plasmon coupling of single gold and silver nanoparticles. *Nat. Biotechnol.* **2005**, *23*, 741–745.

[38] Dolinnyi, A. I. Nanometric rulers based on plasmon coupling in pairs of gold nanoparticles. *J. Phys. Chem. C* **2015**, *119*, 4990–5001.

[39] Göeken, K. L.; Subramaniam, V.; Gill, R. Enhancing spectral shifts of plasmon-coupled noble metal nanoparticles for sensing applications. *Phys. Chem. Chem. Phys.* **2015**, *17*, 422–427.

[40] Chen, H. J.; Kou, X. S.; Yang, Z.; Ni, W. H.; Wang, J. F. Shape- and size-dependent refractive index sensitivity of gold nanoparticles. *Langmuir* **2008**, *24*, 5233–5237.

[41] Fang, Y.; Hoh, J. H. Early intermediates in spermidine-induced DNA condensation on the surface of mica. *J. Am. Chem. Soc.* **1998**, *120*, 8903–8909.

[42] Rubin, R. L. Spermidine-deoxyribonucleic acid interaction *in vitro* and in *Escherichia coli*. *J. Bacteriol.* **1977**, *129*, 916–925.

[43] Vijayanathan, V.; Thomas, T.; Thomas, T. J. DNA nanoparticles and development of DNA delivery vehicles for gene therapy. *Biochemistry* **2002**, *41*, 14085–14094.

[44] Knight, M. W.; Fan, J.; Capasso, F.; Halas, N. J. Influence of excitation and collection geometry on the dark field spectra of individual plasmonic nanostructures. *Opt. Express* **2010**, *18*, 2579–2587.

[45] Jain, P. K.; Huang, W. Y.; El-Sayed, M. A. On the universal scaling behavior of the distance decay of plasmon coupling in metal nanoparticle pairs: A plasmon ruler equation. *Nano Lett.* **2007**, *7*, 2080–2088.

[46] Elhadj, S.; Singh, G.; Saraf, R. F. Optical properties of an immobilized DNA monolayer from 255 to 700 nm. *Langmuir* **2004**, *20*, 5539–5543.

[47] Hurst, S. J.; Lytton-Jean, A. K. R.; Mirkin, C. A. Maximizing DNA loading on a range of gold nanoparticle sizes. *Anal. Chem.* **2006**, *78*, 8313–8318.

[48] Jiang, L. Y.; Yin, T. T.; Dong, Z. G.; Liao, M. Y.; Tan, S. J.; Goh, X. M.; Allioux, D.; Hu, H. L.; Li, X. Y.; Yang, J. K. W. et al. Accurate modeling of dark-field scattering spectra of plasmonic nanostructures. *ACS Nano* **2015**, *9*, 10039–10046.

[49] Tam, F.; Chen, A. L.; Kundu, J.; Wang, H.; Halas, N. J. Mesoscopic nanoshells: Geometry-dependent plasmon resonances beyond the quasistatic limit. *J. Chem. Phys.* **2007**, *127*, 204703.

[50] Brown, K. A.; Park, S.; Hamad-Schifferli, K. Nucleotide-surface interactions in DNA-modified Au-nanoparticle conjugates: Sequence effects on reactivity and hybridization. *J. Phys. Chem. C* **2008**, *112*, 7517–7521.

[51] Van den Broek, B.; Noom, M. C.; van Mameren, J.; Battle, C.; MacKintosh, F. C.; Wuite, G. J. L. Visualizing the formation and collapse of DNA toroids. *Biophys. J.* **2010**, *98*, 1902–1910.

[52] Hulme, E. C.; Trevethick, M. A. Ligand binding assays at equilibrium: Validation and interpretation. *Br. J. Pharmacol.* **2010**, *161*, 1219–1237.